# PROGRESS REPORT

| | |
|---|---|
| Project Title: | Development of Multiobjective Optimization Techniques for Sonic Boom Minimization |
| Grant Number: | NCC2-5064 |
| Principal Investigator: | Dr. Aditi Chattopadhyay<br>Associate Professor<br>Department of Mechanical and Aerospace Engineering<br>Arizona State University |
| Co-Principal Investigator: | Dr. Johnny R. Narayan<br>Research Scientist<br>Aerospace Research Center<br>Arizona State University |
| Graduate Research Assistants: | Mr. Narayanan Pagaldipti<br>Mr. Xu Wensheng<br>Arizona State University |

## OBJECTIVES

The objectives of the current research are as follows.

(a)     Development of a multiobjective optimization procedure for aerospace vehicles with the integration of sonic boom and aerodynamic performance criteria.

(b)     Development of a semi-analytical approach for calculating sonic boom design sensitivities.

## APPROACH

An optimization procedure is developed for the simultaneous improvement of the aerodynamic and sonic boom characteristics of high speed aircraft.  From a sonic boom perspective, it is desirable to minimize the first peak in the overpressure signal at a specified distance away from the aircraft.  From aerodynamics point of view, the aerodynamic drag coefficient to lift coefficient ratio must be minimized while maintaining the lift coefficient at a desired level.  The optimization procedure is applied to wing-body configurations related to high speed aircraft. The details of this optimization problem are described below.

**Optimization Problem**

The optimization problem involves multiple objectives and constraints and can be stated as follows.

Minimize

$$\Delta p_{max} \quad \text{and} \quad C_D/C_L$$

subject to the constraints

$$C_{Lmin} \leq C_L \leq C_{Lmax}$$
$$\Phi_{min} \leq \Phi \leq \Phi_{max}$$

where $\Delta p_{max}$ is the first peak in the overpressure signal at a specified distance from the aircraft, $C_D/C_L$ is the drag to lift ratio, $\Phi$ is the design variable vector and the subscripts "min" and "max" denote lower and upper bounds respectively. Upper and lower bounds are imposed on the design variables during the optimization to prevent unrealistic results. All the design variables that will allow a comprehensive investigation of their individual effects on the overall performance of the aircraft, must be included in the optimization problem.

Since the above optimization problem involves multiple design objectives (two in the present case), traditional optimization techniques which typically consider a single objective function, cannot be used. In the present work, a multiobjective function formulation, based on the Kreisselmeier-Steinhauser (K-S) function approach [1], has been used. This approach is described next.

**Kreisselmeier-Steinhauser (K-S) Multiobjective Formulation**

The K-S function approach helps combine the multiple objective functions and the design constraints into a single composite envelope function which is then minimized using unconstrained techniques. The first step in forming the composite objective function involves the transformation of the original objective functions into reduced objective functions [1]. These reduced objective functions assume the form,

$$F_k^*(\Phi) = 1.0 - \frac{F_k(\Phi)}{F_{k_O}} - g_{max} \leq 0 \qquad k = 1, \dots, NOBJ \tag{1}$$

where $F_{k_O}$ represents the value of the original objective function $F_k$, calculated at the beginning of each optimization cycle. NOBJ denotes the total number of objective functions in the original optimization problem. The quantity $g_{max}$ is the value of the largest constraint of the original optimization problem and is held constant during each cycle. Since the reduced objective functions assume the form of constraints, a new constraint vector $f_m(\Phi)$ (m = 1, 2, ... , NCON+NOBJ, where NCON is the total number of constraints in the original optimization problem) is introduced. The constraint vector includes the original constraints and the constraints introduced by the reduced objective functions (Eq. 1). The new objective function to be minimized is then defined using the K-S function as follows.

$$F_{KS}(\Phi) = f_{max} + \frac{1}{\rho} \log_e \sum_{m=1}^{M} e^{\rho(f_m(\Phi) - f_{max})} \tag{2}$$

where $f_{max}$ is the largest constraint corresponding to the new constraint vector $f_m(\Phi)$ (in general not equal to $g_{max}$). When the original constraints are satisfied during optimization, the constraints due to the reduced objective functions are violated. Initially, in an infeasible design space, where the original constraints are violated, the constraints due to the reduced objective functions (Eq. 1) are satisfied (i.e. $g_{max}$ is negative). The optimizer attempts to satisfy these violated constraints thus optimizing the original objective functions ($F_k$). The multiplier $\rho$, which is analogous to the draw-down factor of penalty function formulation, controls the distance from the surface of the K-S envelope to the surface of the maximum constraint function (Fig. 1). When $\rho$ is large, the K-S function will closely follow the surface of the largest constraint function and when $\rho$ is small, the K-S function will include contributions from all violated constraints with equal weight.

The new unconstrained optimization problem can be solved by using a variety of techniques. In the present work, it is solved using the Broyden-Fletcher-Goldfarb-Shanno (BFGS) algorithm [2]. This algorithm approximates the inverse of the Hessian of the composite objective function

using a rank-two update and guarantees both symmetry and positive definiteness of the updated inverse Hessian matrix.

## Approximation Technique

During the optimization, several evaluations of the objective functions and the constraints need to be done in each optimization cycle. The use of exact analysis to evaluate them at each iteration during an optimization cycle is computationally expensive. Therefore, an approximation technique known as the two-point exponential approximation [3], is used within the optimizer for approximating the objective functions and the constraints. This technique utilizes the gradient of the function with respect to design variables from the current and previous design cycles and is formulated as follows.

$$\hat{F}(\Phi) = F(\Phi_1) + \sum_{n=1}^{NDV} \left[ \left( \frac{\phi_n}{\phi_{1n}} \right)^{p_n} - 1.0 \right] \frac{\phi_{1n}}{p_n} \frac{\partial F}{\partial \phi_n}(\Phi_1) \tag{3}$$

where $\hat{F}(\Phi)$ is the approximation of the function $F(\Phi)$ in the neighborhood of the current design variable vector, $\Phi_1$. The quantity $\phi_n$ is the $n^{th}$ design variable from the design variable vector $\Phi$. NDV is the total number of design variables. The approximate values for the constraints, $\hat{g}_j(\Phi)$, are similarly calculated. The exponent $p_n$ is defined as

$$p_n = \frac{\log_e \left\{ \frac{\left| \frac{\partial F}{\partial \phi_n}(\Phi_0) \right|}{\left| \frac{\partial F}{\partial \phi_n}(\Phi_1) \right|} \right\}}{\log_e \left\{ \frac{\Phi_{on}}{\Phi_{1n}} \right\}} + 1.0 \tag{4}$$

where $\Phi_1$ refers to the design variable vector from the current cycle and $\Phi_0$ denotes the design variable vector from the previous cycle. Equation 3 indicates that in the limiting case of $p_n = 1$, the expansion is identical to the traditional first order Taylor series and when $p_n = -1$, the two-point exponential approximation reduces to the reciprocal expansion form. Therefore, the exponent ($p_n$)

4

can be interpreted as a "goodness of fit" parameter which explicitly determines the trade-off between traditional and reciprocal Taylor series based expansions. $p_n$ is chosen to be within the interval, $-1 \le p_n \le 1$ thus resulting in a hybrid approximation technique.

**Sonic Boom Analysis**

The CFD based analysis procedure for evaluating sonic boom is described in this section. For isentropic flow past smooth axisymmetric bodies, the pressure disturbances (sonic boom) at large distances from the aircraft can be evaluated by using the Whitham F-function [4], which is based on the Abel integral of the equivalent area distribution of the aircraft. Lighthill [5] developed an alternate formulation of the F-function which was shown to be suitable for sonic boom prediction of smooth and non smooth projectile shapes. Walkden extended Whitham's theory [6] for application to wing-body configurations. The asymptotic form of the equations used in developing the sonic boom overpressure signature ($\Delta p/p_\infty$), is as follows.

$$\frac{\Delta p}{p_\infty} = \gamma M_\infty^2 F(y) / \sqrt{2\beta d_0} \qquad (5)$$

$$x = y + \beta d_0 - \kappa \sqrt{d_0} F(y) \qquad (6)$$

$$\beta = (M_\infty^2 - 1)^{0.5} \qquad (7)$$

$$\kappa = (\gamma + 1) M_\infty^4 / [\beta * (2\beta)^{0.5}] \qquad (8)$$

$$\Delta p = (p_{local} - p_\infty), \qquad (9)$$

where F(y) is the Whitham F-function, $\gamma = 1.4$ for air and $M_\infty$ is the freestream Mach number. The equation, $y(x, d_0) = $ constant, is a characteristic curve, x is the streamwise distance and $d_0$ is a specified distance from the flight axis. Since the above mentioned models are based on linearized theory, they fail to agree with wind-tunnel data in highly nonlinear flows such as the flow at angle-of-attack at high Mach numbers ($M_\infty > 2$). Hicks and Mendoza [7] have developed a technique to

5

extrapolate the pressure signature at $d_0$ to a distance $d_1$ ($d_1 > d_0$). First, a pressure signature at distance $d_0$, where the flowfield is assumed to be locally axisymmetric, is directly measured in the wind-tunnel and the value of the F-function (at $d_0$) is evaluated. Since the pressure signal propagates at the local speed of sound and each point of the signal advances according to its amplitude, the signal is distorted as it propagates away from the aircraft and the F-function becomes multivalued. The new F-function at $d_1$ is obtained by placing discontinuities (shocks) in such a way that the discontinuities divide the multivalued regions with equal areas on either side of them. This new F-function gives the overpressure signature at $d_1$ using Eqs. 5 and 6.

Cheung et al. [8] have used a three-dimensional parabolized Navier-Stokes (PNS) code in combination with Whitham's quasilinear theory for sonic boom prediction. The CFD code used in this study, UPS3D, solves the PNS equations governing the flow using an implicit, approximately factored, finite volume algorithm [9]. The flow field associated with wing-body configurations is evaluated and the drag, lift and moment coefficients are computed. Three different approaches have been used by Cheung et al. to obtain the overpressure signal at mid- and far-fields from the near-field CFD solution. One of these three approaches is based on the extrapolation technique described above. In the present work, this extrapolation procedure is used in conjunction with the UPS3D code, to evaluate the sonic boom pressure signatures.

**Aircraft Configuration**

The developed optimization procedure is applied to two different aircraft configurations. The first one, illustrated in Fig. 2, is a delta wing-body configuration and the second one, illustrated in Fig. 3, is a doubly swept wing-body configuration. In both configurations, the centerbody is axisymmetric and is a combination of a nose region and an extended cylindrical region. In the nose region, the radius of the centerbody varies parabolically with the streamwise coordinate over the nose length. The radius of the cylinder is denoted $r_m$. In the nose region, the radius of the body changes from zero (at the tip) to $r_m$ over a nose length, $l_n$, as follows.

6

$$r = r_m - r_m*(1 - x/l_n)^2 \tag{10}$$

Here x is the streamwise distance measured from the nose tip. For the first configuration considered (Fig. 2), the wing planform is delta shaped with a leading edge sweep $\lambda$, root chord $c_0$ and wing span $w_s$. The wing cross section is a symmetric, diamond airfoil (Fig. 2) whose maximum thickness-to-chord ratio is denoted $t_c$. For the second configuration, the wing planform is characterized by a double sweep with sweep angles $\lambda_1$ and $\lambda_2$ and a break length, $x_b$ (Fig. 3). The wing root chord is denoted $c_0$ and tip chord is denoted $c_t$. The wing cross section is a diamond airfoil with thickness-to-chord ratio, $t_c$. For both configurations, the total body length is denoted $l_b$ and the wing starting location is denoted $x_w$.

For the delta wing-body configuration case, the leading edge sweep ($\lambda$), the wing root chord ($c_0$), the wing span ($w_s$), the airfoil thickness-to-chord ratio ($t_c$), the maximum nose radius ($r_m$) and the nose length ($l_n$) are used as design variables. For the doubly swept wing-body configuration case, the two leading edge sweeps ($\lambda_1$ and $\lambda_2$), the break length ($x_b$), the wing root chord ($c_0$), the wing tip chord ($c_t$), the maximum nose radius ($r_m$), the nose length ($l_n$) and the wing starting location ($x_w$) are used as design variables.

## ACCOMPLISHMENTS

Results obtained by using the developed optimization procedure to the configurations described above are presented here. In both cases (delta wing and double sweep), the cruise Mach number is 2.5 and the angle of attack is 5 degrees. The flow field around the vehicle is evaluated using the CFD solver, UPS3D, over a flow domain that extends from the tip of the body up to three times the body length in the axial direction. Currently, the inviscid option is being used within the UPS3D code. The pressure signature is evaluated at a prescribed distance below the vehicle axis and an extrapolation procedure is then used to obtain the pressure signature at desired far-field locations. In the work reported here, the pressure field is evaluated at a distance $d_0 = 0.5$ $l_b$ measured from the axis, directly beneath the aircraft. Optimization is performed for minimum

7

$C_D/C_L$ and minimum sonic boom (overpressure). For the delta wing-body optimization, results are presented for minimum sonic boom at two locations away from the body. The first of the two corresponds to a distance $d_1 = 3.61 \, l_b$ from the axis of the body and is denoted "near-field" in the text. The second distance considered is $d_1 = 941.7 \, l_b$ from the axis of the body and is denoted "far-field" in the text. For the doubly swept wing-body configuration, only results from the far-field case of $d_1 = 941.7 \, l_b$ are presented.

**Delta Wing-Body Optimization**

The initial choice of the design variables (reference values) are: wing root chord $(c_0) = 7.08$ m, leading edge sweep $(\lambda) = 66.0$ degrees, wing half span $(w_s) = 3.53$ m, wing thickness to chord ratio $(t_c) = 0.052$, maximum radius of the nose section $(r_m) = 0.57$ m and nose length $(l_n) = 6.01$ m. The wing starting location $(x_w) = 8.21$ m and is held constant during the optimization.

<u>Near-Field Sonic Boom Minimization</u>

The results from the optimization of the pressure signature at a distance of $3.61 \, l_b$ are presented here. Results from two sets of optimization are presented. In the first case, the optimization is performed for minimum $C_D/C_L$ and minimum sonic boom (overpressure) with a constraint on the lift coefficient. The lift coefficient in this case is constrained using $C_{L_{min}} = C_{L_{ref}}$ and $C_{L_{max}} = 1.02 C_{L_{ref}}$ where $C_{L_{ref}}$ is the lift coefficient of the reference configuration. Table 1 compares the sonic boom overpressure (first and second peaks), drag coefficient and lift coefficient respectively, for the reference and the optimum delta wing configurations. The first peak in the pressure signature decreases significantly, by 11.1 percent, for the optimum configuration. The second peak in the pressure signature increases by 2.9 percent. The drag-to-lift ratio decreases by 4.3 percent and the drag coefficient decreases by 3.7 percent. There is an increase in the lift coefficient in the optimized configuration (0.7 percent). Table 2 compares the reference and the optimum values of the six design variables used in the optimization. Significant reductions are observed in the wing thickness-to-chord ratio and nose radius whereas the nose length and the

8

wing root chord have increased. Small changes in the leading edge sweep and wing half span are observed. Figure 4 presents the reference and optimum pressure distributions at $d_1 = 3.61$ $l_b$. As shown, there is a significant reduction in the first peak of the pressure signature for the optimum configuration. Figure 5 presents the geometries for the reference and the optimum configuration and clearly depicts the changes in the design variables. As a second case, the optimization is performed for minimum $C_D/C_L$ and minimum sonic boom without constraint imposed on the lift coefficient. This is done in order to investigate the design trade-off between improvements in sonic boom and wing lifting capabilities. Table 3 compares the values of the sonic boom overpressure (first and second peaks), drag coefficient and lift coefficient respectively, for the reference and the optimum delta wing configurations. The first peak in the pressure signature decreases significantly by 21.5 percent for the optimum configuration. The second peak in the pressure signature decreases by 2.4 percent. The drag-to-lift ratio decreases by 7.1 percent and the drag coefficient decreases by 11.9 percent. However, there is a decrease in the lift coefficient of the optimized configuration (5.0 percent). Table 4 compares the reference and the optimum values of the six design variables used in the optimization. Significant reductions are observed in the wing thickness-to-chord ratio and nose radius whereas nose length and wing root chord have increased. Small changes in the leading edge sweep and wing half span are observed. Figure 6 presents the reference and optimum pressure distributions at $d_1 = 3.61$ $l_b$. There is a significant reduction in both the peaks of the pressure signature for the optimum configuration. Figure 7 presents the geometries for the reference and the optimum configuration and the changes in the design variables can once again be observed. These changes, especially the reduction in the dimensions of the aircraft nose and the wing thickness-to-chord ratio, cause reductions in the sonic boom overpressure and the drag coefficient. The reduction in the lift coefficient may be due to the slight decrease in the wing planform area associated with the changes in the root chord, nose length, nose radius and the wing half span.

The two optimum design cases considered reveal an important trend. In the first case where a constraint on the lift coefficient is imposed, the optimum design has an improved lift coefficient.

The sonic boom signature associated with this design is also reduced, however, an increase in the second peak is observed which is not so critical from sonic boom stand point. In the second case where no constraint is imposed on the lift coefficient, the reduction in the first peak is very significant (compared to the optimum from the previous case) and the second peak is also reduced. However, the lift coefficient is decreased. The optimum design also has much improved $C_D$ and $C_D/C_L$ values compared to the optimum design from the previous case. Thus the strong trade-off between sonic boom overpressure and lift enhancement is observed. This is due to the fact that both sonic boom overpressures and induced drag increase with an increase in the lift and decrease with a decrease in the lift. The optimization procedure, in the second case, exploits this important physical relationship and yields significantly low boom configurations with reduced $C_L$.

Far-Field Sonic Boom Minimization

The results from the optimization of the pressure signature at a distance of 941.7 $l_b$ are presented next. The optimization is performed for minimum sonic boom and minimum $C_D/C_L$ without constraint on the lift coefficient. Table 5 compares the values of the sonic boom overpressure, drag coefficient and lift coefficient respectively, for the reference and the optimum delta wing configurations. The first peak in the pressure signature decreases by 10.2 percent and the second peak increases by 0.4 percent for the optimum configuration. The drag-to-lift ratio is decreased by 6.0 percent and the drag coefficient has decreased by 9.7 percent. The lift coefficient is also decreased by 3.9 percent. Table 6 compares the reference and the optimum values of the six design variables used in the optimization. Significant reductions are observed in the wing thickness-to-chord ratio, wing span and nose radius whereas the wing root chord and nose length have increased. Figure 8 presents the pressure signatures for the reference and optimum configurations at $d_1 = 941.7$ $l_b$, respectively. The significant reduction in the first peak of the pressure signature can be clearly seen in this figure. Figure 9 compares the reference and optimum geometries. The significant changes to the design variables can be seen from this figure.

10

In both near-field and far-field sonic boom optimizations, it is observed that the multiobjective optimization procedure yields designs where the drag and sonic boom characteristics are significantly improved. However, in the absence of a constraint on the lift coefficient, these improvements are associated with small penalties in the lift, as expected.

A comparison of the quality of the optimum designs obtained through the near-field and far-field sonic boom optimizations is made. Figure 10 presents the pressure signatures of the optimum configurations obtained from the near-field and far-field wave minimizations at a distance, $d_1 = 941.7$ $l_b$. It is observed that the near-field optimum has a better first peak than the far-field optimum at this distance $d_1$. In fact, the near-field signature has a first peak 1.9 percent lesser than the far-field signature. However, the second peak of the near-field wave is higher than the far-field optimum by 3.9 percent.

Doubly Swept Wing-Body Optimization

The initial choice of the design variables (reference values) are: wing root chord ($c_o$) = 8.08 m, wing tip chord ($c_t$) = 1.70 m, first leading edge sweep ($\lambda_1$) = 69.0 degrees, second leading edge sweep ($\lambda_2$) = 55.0 degrees, wing starting location ($x_w$) = 8.21 m, break length ($x_b$) = 12.0 m, maximum radius of the nose section ($r_m$) = 0.57 m and nose length ($l_n$) = 6.01 m. The wing half span ($w_s$) = 3.45 m and the wing thickness to chord ratio ($t_c$) = 0.052 and are held constant during the optimization. Optimization is performed for minimum $C_D/C_L$ and minimum sonic boom (overpressure) at a far-field distance $d_1$ = 941 $l_b$. The lift coefficient is constrained using $C_{L_{min}} = C_{L_{ref}}$ and $C_{L_{max}} = 1.05$ $C_{L_{ref}}$ where $C_{L_{ref}}$ is the lift coefficient of the reference configuration.

The results from the optimization procedure are presented in Table 7. The data for the reference and two difference optimum designs are shown. The two optimum results correspond to two different local minima. Optimum design 1 is obtained after eight cycles and optimum design 2 is achieved after six cycles. As shown in Table 7, significant improvements are observed in the objective functions and the constraint after optimization. However, a larger reduction (2.3 percent)

11

in the maximum overpressure and a more significant increase in the lift coefficient (4.7 percent) is observed in Optimum 2. The reduction in drag-to-lift ratio is more significant (3.5 percent) in Optimum 1. It is also interesting to note that in this case, the value of $C_D$, which is not used as a design objective or a constraint, also reduces significantly (1.8 percent). The importance of the different geometric parameters used as design variables, towards the optimum design under the given set of objectives and constraints is demonstrated in Table 8. For example, for this optimization problem, the geometric parameters that change most are associated with the nose section ($l_n$ and $r_m$). Figure 11 presents the reference and optimum pressure distributions at $d_1 = 941 l_b$. Figure 12 presents the geometries for the reference and the two optimum configurations. The changes in the design variables, especially the reduction in the dimensions of the aircraft nose, cause reductions in the sonic boom overpressure and the drag coefficient. The increase in the lift coefficient is due to the slight decrease in the wing planform area of the optimum configuration. The extent of reduction in the wing planform area is slightly more significant than the decrease in the actual lift thus resulting in an increase in the lift coefficient.

It is also observed that the percentage improvements in the drag coefficient, lift coefficient and the sonic boom overpressure peak, for the doubly swept wing-body configuration, are much smaller in magnitude than the corresponding improvements for the delta wing-body configuration. One of the main reasons for this trend is the fact that, during the doubly swept wing-body optimization, the wing thickness-to-chord ratio is not included as a design variable and is held fixed during the optimization. The wing thickness-to-chord ratio, which is included as a design variable in the delta wing-body optimization, is significantly decreased along with the nose radius during the optimization which results in the significant improvements observed in the drag-to-lift ratio and the sonic boom overpressure peak in the delta wing-body case.

The multiobjective optimization procedure is efficient and is capable of producing designs that represent the best compromise between the conflicting performance criteria. The approximate analysis procedure used within the optimizer yields sufficiently accurate values for the objective functions and constraints and results in significant computational savings.

# SIGNIFICANCE OF THE PRESENT RESEARCH

A multiobjective optimization procedure has been developed for minimizing sonic boom and improving aerodynamic performance of high speed aircraft. The procedure consists of a multiobjective optimization technique, a CFD solver and an extrapolation technique for evaluating sonic boom pressure signatures. The multiobjective problem is formulated using the Kreisselmeier-Steinhauser function approach. Aerodynamic performance enhancement and sonic boom reduction were the primary objectives that formed the bases of this study. The aircraft geometric parameters were used as design variables. A three-dimensional parabolized Navier-Stokes solver (UPS3D) is used for performing aerodynamic analysis and an extrapolation procedure based on Whitham's theory is used for performing sonic boom analysis. The optimization procedure has been applied to two generic high speed configurations: (a) delta wing-body configuration and (b) doubly swept wing-body configuration. The following observations can be made from this study.

1.  The multiobjective optimization procedure is efficient and yields overall improvements in all the performance criteria included in the formulation.

2.  The approximate analysis procedure used to evaluate objective functions and constraints within the optimizer is accurate and yields significant computational savings.

3.  The procedure demonstrates a definite trade-off between low boom and high lift designs.

4.  The optimization procedure helps in identifying the important parameters (e.g., nose dimensions) that are critical in achieving the desired design objectives.

The optimization procedure that has been developed is useful in a number of stages of the design process. It is useful in a design trade-off study. It helps to identify the critical parameters that influence the design objectives. It is useful to optimize an existing or preliminary design to achieve the overall design objectives. It is capable of handling multiple design objectives that may originate in different disciplines associated with the overall design. It is also modular in structure thus enabling the inclusion of different disciplines during the various stages of the design process.

# REFERENCES

1. Kreisselmeier, A. and Steinhauser, R., "Systematic Control Design by Optimizing a Vector Performance Index," *Proceedings of the IFAC Symposium on Computer Aided Design of Control Systems*, Zurich, Switzerland, 1979, pp. 113-117.

2. Haftka, R. T., Gurdal, Z. and Kamat, M. P., "Elements of Structural Optimization," *Kluwer Academic Publishers*, Dordrecht, The Netherlands, 1990.

3. Fadel, G. M., Riley, M. F. and Barthelemy, J. F. M., "Two-Point Exponential Approximation Method for Structural Optimization," *Structural Optimization, 2*, 1990, pp. 117-124.

4. Whitham, G. B., "The Flow Pattern of a Supersonic Projectile," *Communications on Pure and Applied Mathematics*, Vol. 5, No. 3, 1952, pp. 301-348.

5. Lighthill, M. J., "General Theory of High Speed Aerodynamics, Sec. E; see also High Speed Aerodynamics and Propulsion," Vol. 6, Princeton University Press, NJ, 1954, pp. 345-389.

6. Walkden, F., "The Shock Pattern of a Wing-Body Combination, Far from the Flight Path," *Aeronautical Quarterly*, Vol. 9, Pt. 2, May 1958, pp. 164-194.

7. Hicks, R. and Mendoza, J., "Prediction of Aircraft Sonic Boom Characteristics from Experimental Near-Field Results," *NASA TMX-1477*, November, 1967.

8. Cheung, S. H., Edwards, T. A. and Lawrence, S. L., "Application of Computational Fluid Dynamics to Sonic Boom Near- and Mid-Field Prediction," *Journal of Aircraft*, Vol. 29, No. 2, 1992, pp. 920-926.

9. Lawrence, S., Chaussee, D. and Tannehill, J., "Application of an Upwind Algorithm to the 3-D Parabolized Navier-Stokes Equations," AIAA Paper 87-1112, June 1987.

10. Narayan, J. R., Chattopadhyay, A., Pagaldipti, N. and Cheung, S. H., "Optimization Procedure for Improved Sonic Boom and Aerodynamic Performance Using a Multiobjective Formulation Technique," AIAA Paper 95-0127, *33rd Aerospace Sciences Meeting and Exhibit*, Reno, Nevada, January 1995.

11. Chattopadhyay, A., Narayan, J. R., Pagaldipti, N., Wensheng, X. and Cheung, S. H., "Optimization Procedure for Reduced Sonic Boom in High Speed Flight," AIAA Paper 95-2156, *26th AIAA Fluid Dynamics Conference,* San Diego, California, June, 1995.

Table 1. Comparison of objective functions; near-field case with lift constraint

| Performance functions | Reference Design | Optimum Design | Percentage change |
|---|---|---|---|
| Drag coefficient, $C_D$ | 0.02446 | 0.023566 | -3.7 |
| Lift coefficient, $C_L$ | 0.20940 | 0.21080 | +0.7 |
| Drag-to-lift ratio, $C_D/C_L$ | 0.11681 | 0.11179 | -4.3 |
| Max. overpressure (I peak) | 0.033195 | 0.029506 | -11.1 |
| Max. overpressure (II peak) | 0.058379 | 0.060101 | +2.9 |

Table 2. Comparison of design variables; Near-field case with lift constraint

| Design Variables | Reference | Optimum |
|---|---|---|
| Root chord, $c_0$ (m) | 7.08 | 7.11 |
| Leading edge sweep, $\lambda$ (deg) | 66.0 | 64.8 |
| Thickness to chord ratio, $t_c$ | 0.05200 | 0.04894 |
| Wing half span, $w_s$ (m) | 3.53 | 3.4964 |
| Nose length, $l_n$ (m) | 6.01 | 6.3799 |
| Max. nose radius, $r_m$ (m) | 0.570 | 0.5364 |

Table 3. Comparison of performance functions; near-field case without lift constraint

| Performance functions | Reference Design | Optimum Design | Percentage change |
|---|---|---|---|
| Drag coefficient, $C_D$ | 0.02446 | 0.02155 | -11.9 |
| Lift coefficient, $C_L$ | 0.20940 | 0.19894 | -5.0 |
| Drag-to-lift ratio, $C_D/C_L$ | 0.11681 | 0.10855 | -7.1 |
| Max. overpressure (I peak) | 0.033195 | 0.026046 | -21.5 |
| Max. overpressure (II peak) | 0.058379 | 0.056991 | -2.4 |

Table 4. Comparison of design variables; near-field case without lift constraint

| Design Variables | Reference | Optimum |
|---|---|---|
| Root chord, $c_0$ (m) | 7.08 | 7.34 |
| Leading edge sweep, $\lambda$ (deg) | 66.0 | 66.5 |
| Thickness to chord ratio, $t_c$ | 0.05200 | 0.04680 |
| Wing half span, $w_s$ (m) | 3.530 | 3.425 |
| Nose length, $l_n$ (m) | 6.01 | 6.611 |
| Max. nose radius, $r_m$ (m) | 0.570 | 0.513 |

Table 5. Comparison of performance functions; far-field case without lift constraint

| Performance functions | Reference Design | Optimum Design | Percentage change |
|---|---|---|---|
| Drag coefficient, $C_D$ | 2.4460E-02 | 2.2099E-02 | -9.7 |
| Lift coefficient, $C_L$ | 2.0940E-01 | 2.0117E-01 | -3.9 |
| Drag-to-lift ratio, $C_D/C_L$ | 1.1681E-01 | 1.0985E-01 | -6.0 |
| Max. overpressure (I peak) | 1.9479E-03 | 1.7499E-03 | -10.2 |
| Max. overpressure (II peak) | 3.3102E-03 | 3.3220E-03 | 0.4 |

16

Table 6. Comparison of design variables; far-field case without lift constraint

| Design Variables | Reference | Optimum |
|---|---|---|
| Root chord, $c_0$ (m) | 7.08 | 7.64 |
| Leading edge sweep, $\lambda$ (deg) | 66.0 | 67.1 |
| Thickness to chord ratio, $t_c$ | 0.05200 | 0.04680 |
| Wing half span, $w_s$ (m) | 3.53 | 3.2164 |
| Nose length, $l_n$ (m) | 6.01 | 6.6042 |
| Max. nose radius, $r_m$ (m) | 0.570 | 0.5514 |

Table 7. Comparison of performance functions

| Performance functions | Reference Design | Optimum 1 | Optimum 2 |
|---|---|---|---|
| Drag coefficient, $C_D$ | 0.012849 | 0.0126160 (-1.8%) | 0.0130655 (+1.7%) |
| Lift coefficient, $C_L$ | 0.11085 | 0.11274 (+1.7%) | 0.116094 (+4.7%) |
| Drag-to-lift ratio, $C_D/C_L$ | 0.11592 | 0.11190 (-3.5%) | 0.11260 (-2.8) |
| Max. overpressure | 0.0019092 | 0.0018758 (-1.7%) | 0.0018660 (-2.3%) |

Table 8. Comparison of design variables

| Design Variables | Reference | Optimum 1 | Optimum 2 |
|---|---|---|---|
| 1st leading edge sweep, $\lambda_1$ (deg) | 69.00 | 70.16 | 69.80 |
| Root chord, $c_0$ (m) | 8.08 | 8.12 | 7.94 |
| 2nd leading edge sweep, $\lambda_2$ (deg) | 55.00 | 54.93 | 55.10 |
| Root chord, $c_t$ (m) | 1.7000 | 1.6191 | 1.6300 |
| Nose length, $l_n$ (m) | 6.01 | 6.5976 | 6.3100 |
| Maximum nose radius, $r_m$ (m) | 0.5400 | 0.4971 | 0.5100 |
| Break length, $x_b$ (m) | 12.00 | 12.28 | 12.30 |
| Wing starting location, $x_w$ (m) | 8.21 | 8.13 | 8.17 |
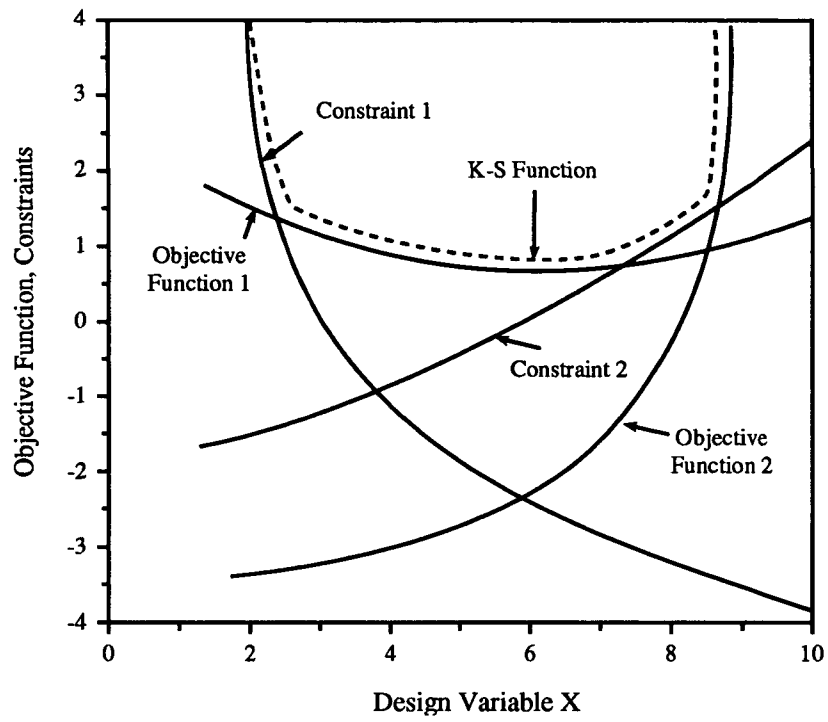
Figure 1.  Kreisselmeier-Steinhauser function envelope

Diamond airfoil (Section AA)
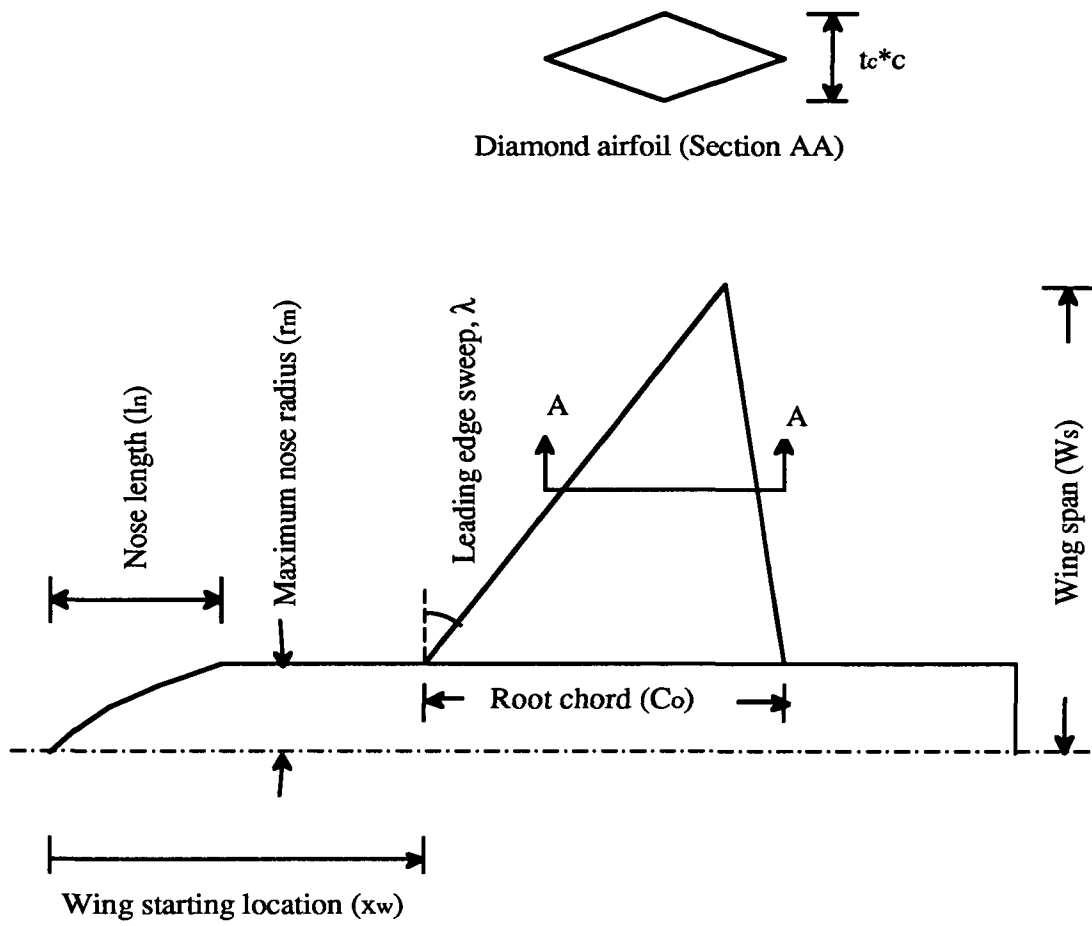


Figure 2. Design variables for the delta wing-body configuration
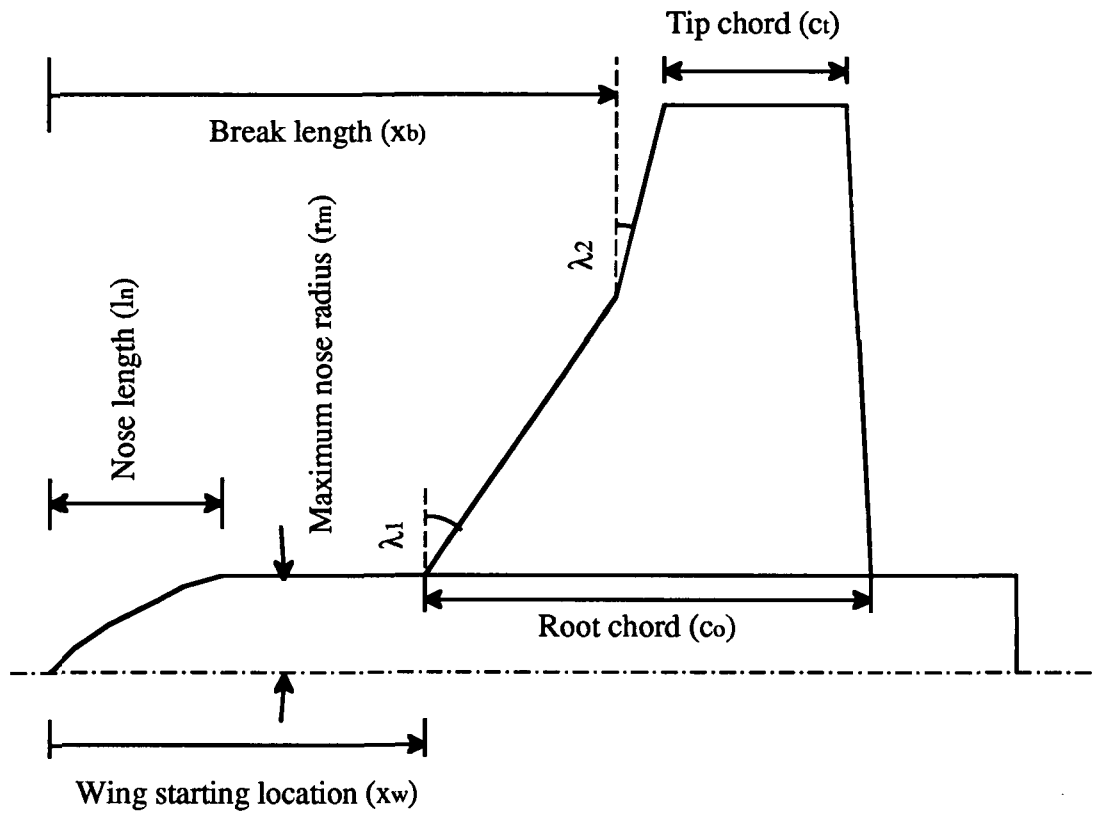
Figure 3. Double sweep wing-body configuration
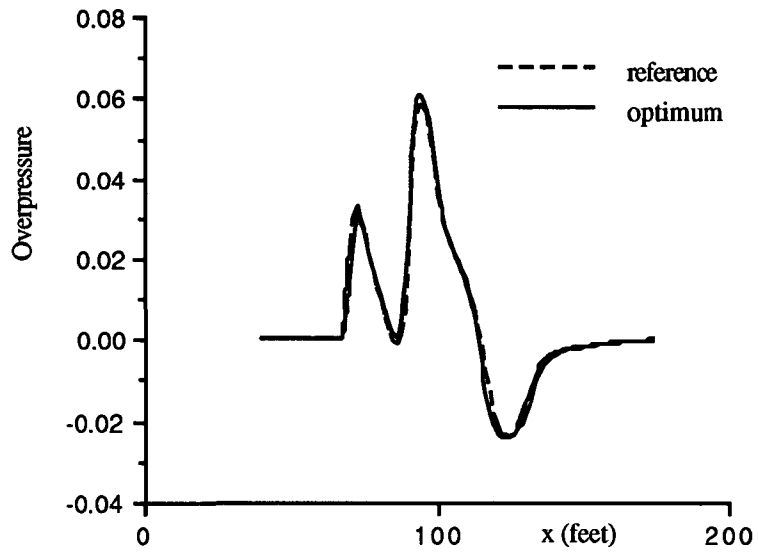
Figure 4. Comparison of pressure signatures; near-field case with lift constraint
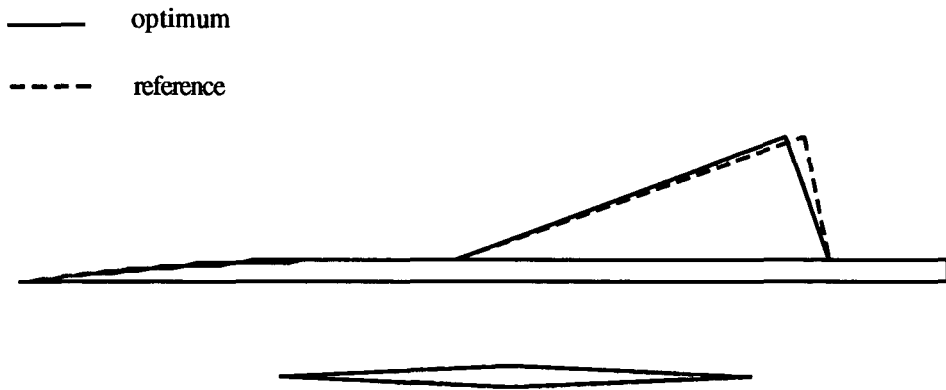
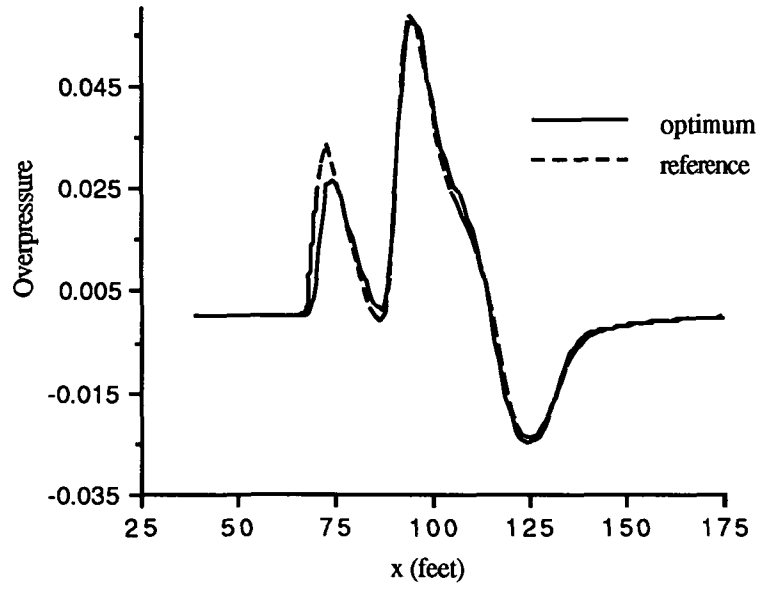Figure 5. Comparison of geometries; near-field case with lift constraint

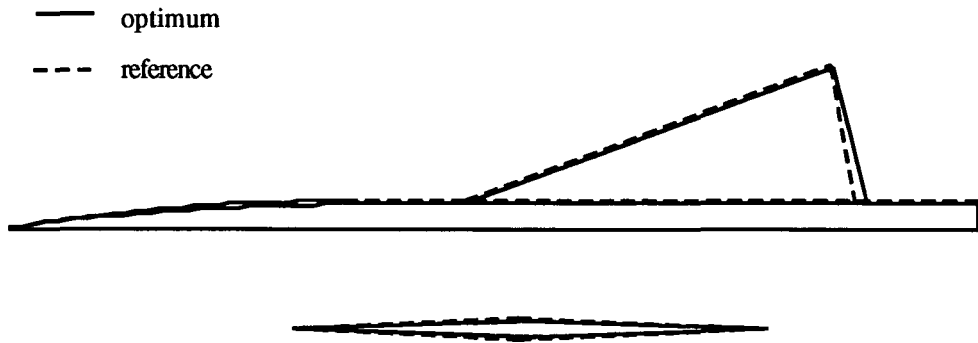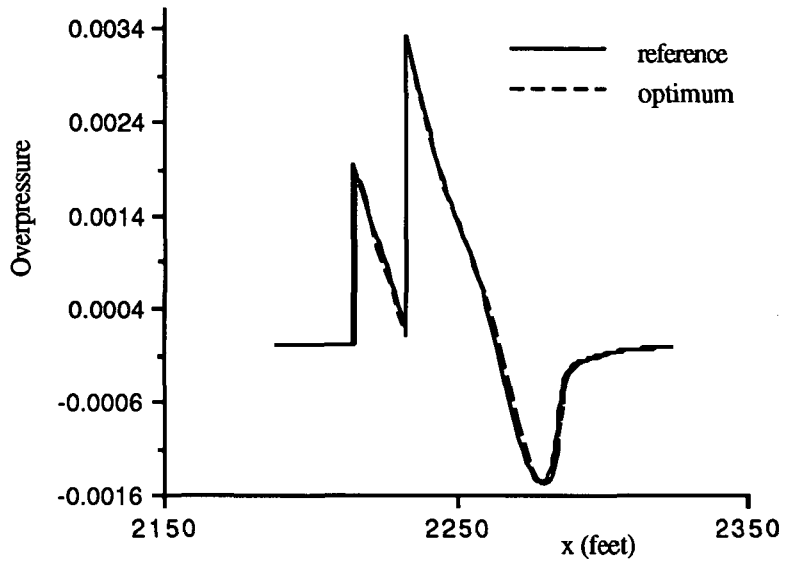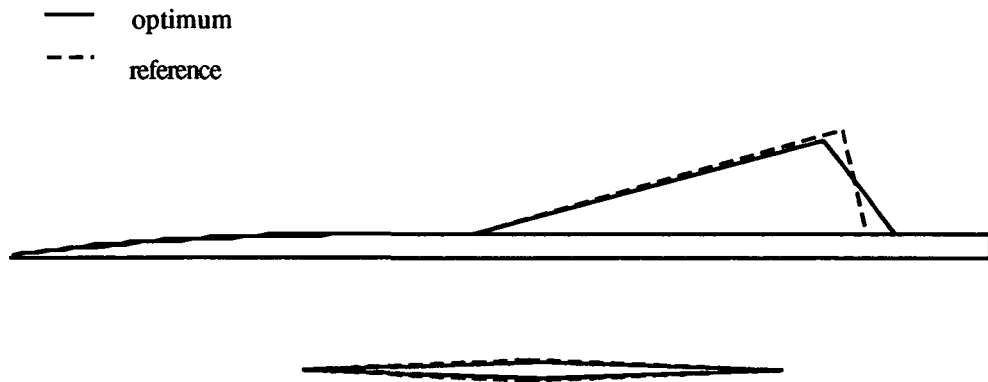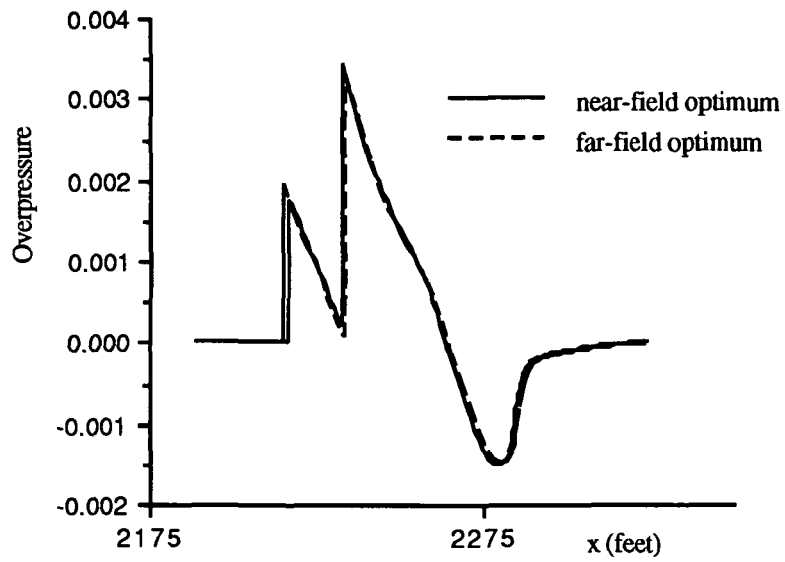Figure 6. Comparison of pressure signatures; near-field case without lift constraint

optimum

- - - reference

Figure 7.  Comparison of geometries; near-field case without lift constraint

Figure 8. Comparison of pressure signatures; far-field case without lift constraint

— optimum

- - · reference

Figure 9. Comparison of geometries; far-field case without lift constraint

Figure 10. Comparison of near-field and far-field optimum pressure signatures at $d_1 = 941.7 \, l_b$

27
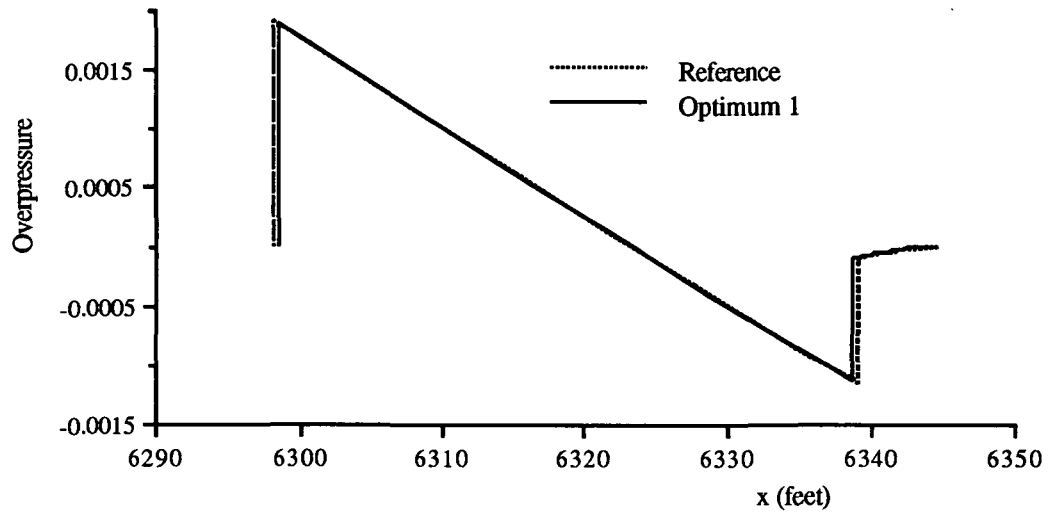
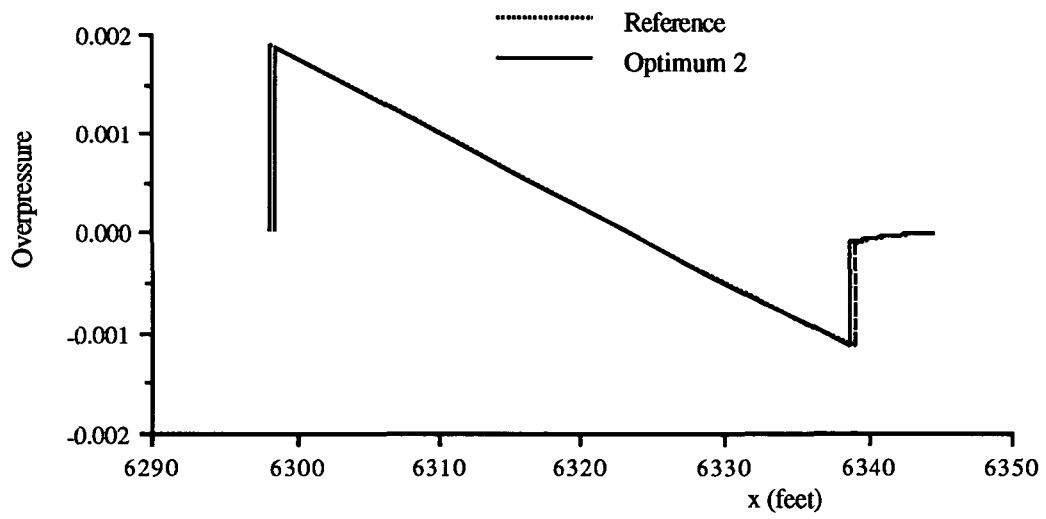Figure 11a. Comparison of pressure signatures for reference and first optimum configurations

Figure 11b. Comparison of pressure signatures for reference second optimum configurations
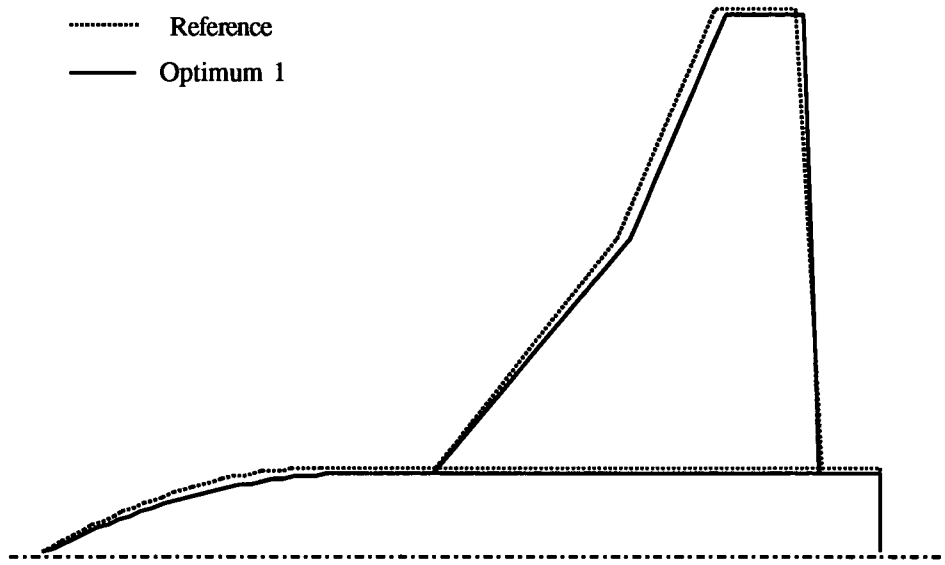
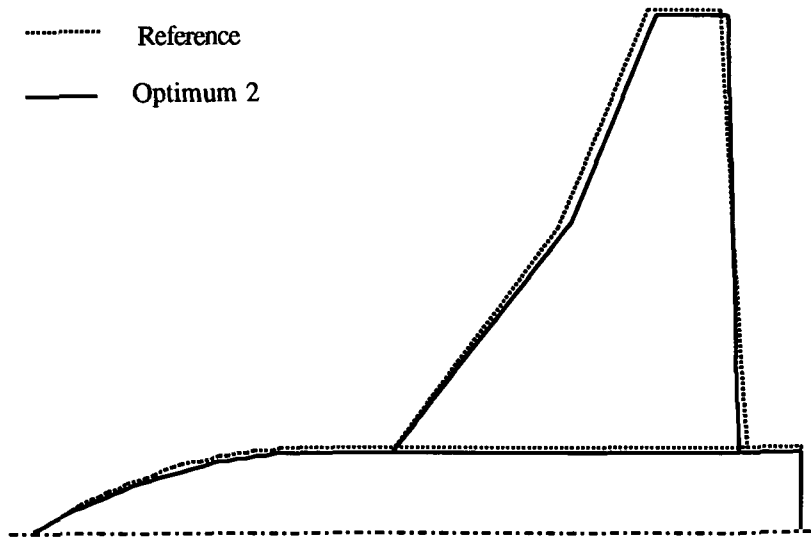Figure 12a. Comparison of reference and first optimum configurations

Figure 12b. Comparison of reference and the second optimum configurations